J Mater Sci (2018) 53:4582–4597

Metals

Deformation and damage of sintered low-porosity aluminum under planar impact: microstructures and mechanisms

Y. Yao[1,2], H. W. Chai[2], C. Li[2], B. X. Bie[1,2], X. H. Xiao[3], J. Y. Huang[2,*], M. L. Qi[1,*], and S. N. Luo[2,4,*]

[1] School of Science, Wuhan University of Technology, Wuhan 430070, Hubei, People's Republic of China
[2] The Peac Institute of Multiscale Sciences, Chengdu 610031, Sichuan, People's Republic of China
[3] Advanced Photon Source, Argonne National Laboratory, Argonne, IL 60439, USA
[4] Key Laboratory of Advanced Technologies of Materials, Ministry of Education, Southwest Jiaotong University, Chengdu 610031, Sichuan, People's Republic of China

Received: 19 September 2017
Accepted: 27 November 2017
Published online: 4 December 2017

ABSTRACT

Plate impact experiments are conducted to study compaction and spallation of 5% porosity aluminum. Free surface velocity histories, the Hugoniot elastic limit (HEL), and spall strengths are obtained at different peak stresses and pulse durations. Scanning electron microscopy, electron backscatter diffraction, and X-ray computed tomography are used to characterize 2D and 3D microstructures. 3D void topology analyses yield rich information on size distribution, shape, orientation, and connectivity of voids. HEL decreases/increases with sample thickness/impact velocity and approaches saturation. Its tensile strength increases with increasing peak stress and shock-induced densification. With the enhanced compaction under increasing impact velocities, spall damage modes change from growth of original voids to inter-particle crack propagation and to "random" nucleation of new voids. Such a change in damage mechanism also gives rise to a distinct decrease in damage extent at high impact velocities. Compaction induces strain localizations around the original voids, while subsequent tension results in grain refinement, and shear deformation zones between staggered cracks.

Introduction

Development of powder metallurgy including sintering makes it possible to produce porous bulk materials economically, with a full control of composition and production rates [1, 2]. Powder-sintered, low-porosity aluminum (e.g., $< 5\%$) is of increasing interest regarding achieving a balanced strength, density, and energy absorption for engineering applications [3, 4]. In addition, low-porosity aluminum, with randomly distributed small pores, is a model material for investigating microstructure

Address correspondence to E-mail: jyhuang@pims.ac.cn; emmy_qi@163.com; sluo@pims.ac.cn

https://doi.org/10.1007/s10853-017-1869-9

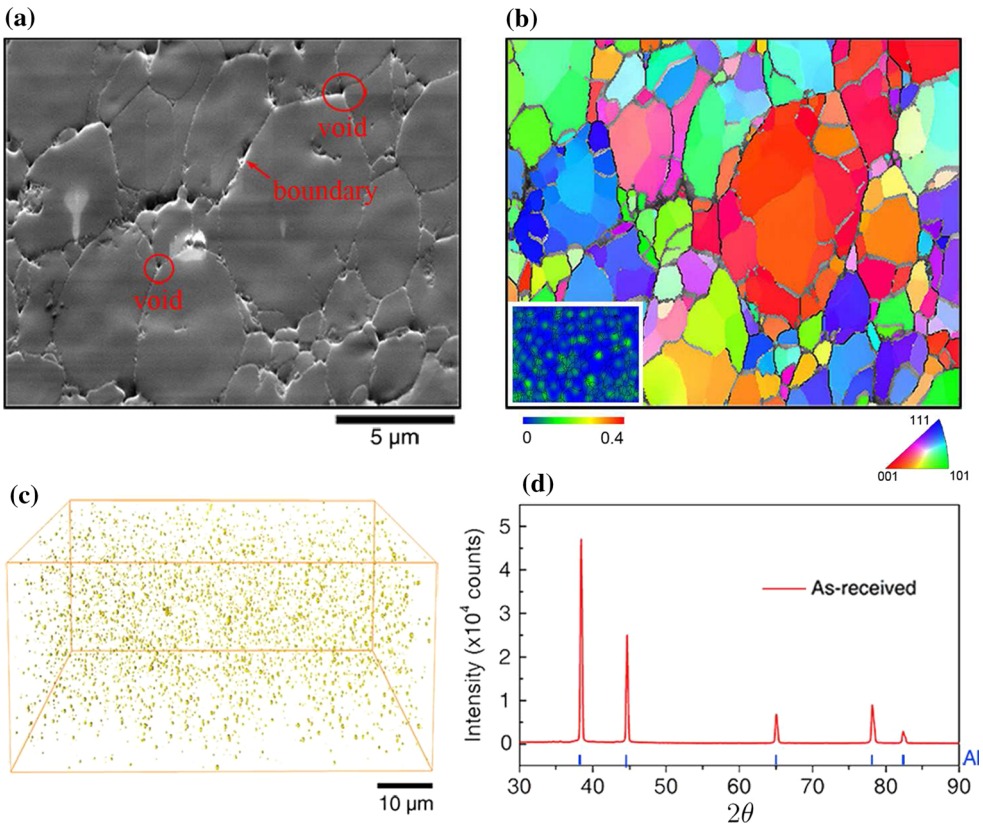

Figure 1 **a** SEM micrograph showing particle boundaries and voids and **b** corresponding EBSD inverse pole figure map of the as-received porous aluminum sample, showing grain boundaries within a single particle. The corresponding strain contour map is shown in the inset. **c** X-ray tomography characterization of the as-received aluminum sample; only voids are shown. **d** X-ray diffraction pattern of the as-received aluminum obtained with a Cu K_α X-ray source.

effects on mechanical properties under various loading conditions including impact [5, 6] and irradiation damage [4, 7], and underlying mechanisms.

Shock experiments have been conducted on low-porosity aluminum at very high impact velocities [3, 8, 9] which are actually not feasible to resolve the pore compaction and collapse dynamics. Wang et al. [3, 9] studied the dynamic compaction and spall fracture of 3% porosity aluminum at impact velocities above 0.3 km s^{-1}, mainly relying on the particle velocity profiles. The spall strength of porous aluminum is apparently lower than that of dense solids and increases with increasing peak stress. It is believed that pores serve as effective sources of shock attenuation [10, 11] and thus play a key role in the Hugoniot elastic limit (HEL) and spall strength. However, the shock-induced pore compaction dynamics and the effects of loading conditions (e.g., peak stress and pulse duration) [12] have not been fully investigated for low-porosity aluminum.

Previous studies have largely focused on the macroscopic mechanical measurements under shock loading with velocity/displacement interferometry [3, 8, 12, 13]. Microscopic characterizations such as electron backscattering diffraction (EBSD) [14, 15] and X-ray computed tomography (XCT) [16–18] are rarely combined to characterize the multi-scale structural evolution of porous metals. Therefore, deformation and damage mechanisms, e.g., nucleation and growth of initial or new voids, and inter-granular/particle or trans-granular/particle fracture modes [19, 20], have not been fully understood. X-ray computed tomography (XCT) [18] has proved its strong capability of resolving 3D microstructures of materials, such as pores, cracks, and second-phase particles [18, 21]. Joint use of such techniques as scanning electron microscope (SEM), EBSD, and XCT is advantageous in quantitative analyses of the multi-scale structure–property relationships of porous aluminum [15].

In this work, we conduct plate impact experiments to investigate shock compaction and spallation of sintered, low-porosity (5%) aluminum, for different impact velocities and pulse durations. Free surface velocity histories are measured for deriving the Hugoniot elastic limit (HEL), spall strengths and damage dynamics. EBSD and XCT are adopted to characterize 2D and 3D microstructures of the initial

Table 1 Experimental parameters

Experimental group	Shot #	L_f (mm)	L_s (mm)	u_f (m s^{-1})	τ (μs)	Δu_{fs} (m s^{-1})	σ_{HEL} (GPa)	σ_H (GPa)	σ_{sp} (GPa)	a_r (m s^{-2})
Peak stress	LP190	0.60	1.06	102	0.068	44	0.08	0.54	0.32	146
	LP189	0.60	1.07	134	0.081	52	0.16	0.89	0.37	− 120
	LP167	0.59	1.04	174	0.084	54	0.16	1.11	0.40	− 281
	LP193	0.61	1.10	213	0.091	59	0.16	1.44	0.43	− 136
	LP401	0.58	1.05	294	0.088	63	0.16	1.98	0.46	− 209
Pulse duration	LP502	0.29	0.60	204	0.012	62	0.25	1.37	0.45	− 674
	LP198	0.61	1.08	187	0.086	56	0.16	1.23	0.41	− 205
	LP601	0.91	1.80	192	0.126	62	0.16	1.31	0.45	− 40

L_f, flyer plate thickness; L_s, sample thickness; u_f, flyer velocity; τ, pulse duration; Δu_{fs}, pullback velocity; σ_{HEL}, Hugoniot elastic limit; σ_H, Hugoniot or peak stress; σ_{sp}, spall strength; a_r, re-acceleration

materials and recovered samples. EBSD reveals deformation characteristics including compaction, shear strain localization, and grain refinement. XCT yields complete void configurations, and a thorough void topology analysis is performed. Connections are made among macroscopic phenomena, microscopic deformation and damage characteristics, and deformation and damage mechanisms. Section 2 addresses materials and experimental details. Section 3 presents results and relevant discussions, including bulk shock and spallation properties, the effects of peak stress and pulse duration, and microstructure analyses, followed by a summary in Sect. 4.

Materials and experiments

The samples (as well as flyer plates) for impact experiments are prepared from porous aluminum with an initial porosity of ~ 5% and a bulk density $\rho_0 \sim 2.58$ g cm^{-3}. This commercial low-porosity aluminum is fabricated via sintering 99.9% pure, solid-phase aluminum powders with negligible oxidization. Under ambient conditions, its longitudinal (C_l) and transverse sound velocities are obtained with ultrasonic measurements, being 6156 and 3096 m s^{-1}, respectively; the corresponding bulk sound speed (C_b) is 5012 m s^{-1}, and Poisson's ratio is 0.33.

Microstructure of the as-received porous aluminum is examined with SEM and EBSD. Figure 1 shows particle boundaries, voids, and grain boundaries within a single particle. The particle size ranges from 2 to 15 μm, with an average particle size of ~ 6 μm. The EBSD inverse pole figure map (Fig. 1b) reveals particle boundaries as well as grain and subgrain (<5°) boundaries within individual particles, with negligible texture. The strain contour map corresponding to Fig. 1b is shown in the inset; slight strain localizations are observed around subgrain boundaries, probably due to compression and sintering. The number and amplitude of strain localizations increase with increasing impact velocity The spatial distribution of voids obtained from XCT is presented in Fig. 1c. They are mostly less than 3 μm in diameter, occurring randomly at the junctions of three or more particles, and are presumably a key role in shock response, including compaction and spall fracture [13]. The XCT measurements are performed at the beamline 2-BM at the Advanced Photon Source with a resolution limit of 0.87 μm, and the details were presented elsewhere [22]. X-ray diffraction pattern (Fig. 1d) of the as-received sample demonstrates its high purity, and the amount of Al_2O_3 impurity is negligible.

In order to explore deformation and damage of this low-porosity aluminum under high strain-rate loading, we perform plate impact experiments using a 14-mm bore diameter single-stage gas gun [23]. The schematic setup of the impact experiments is shown in Fig. 2a. A flyer plate (3) is attached to a polycarbonate sabot (1), with a recess (2) immediately behind it. When a solenoid valve is fired, compressed gas (N_2 or He) is released from a high-pressure gas reservoir into the gun barrel (9), accelerating the sabot and flyer plate assembly. Upon exiting the muzzle, the flyer plate impacts the target sample under consideration (4). The flyer plate velocity is measured with an optical beam blocking system (8) and the free surface velocity u_{fs} of the target with a photon Doppler velocimeter or PDV (7) [24]. The muzzle, target, and PDV probes including related optics are located in a vacuum chamber (10).

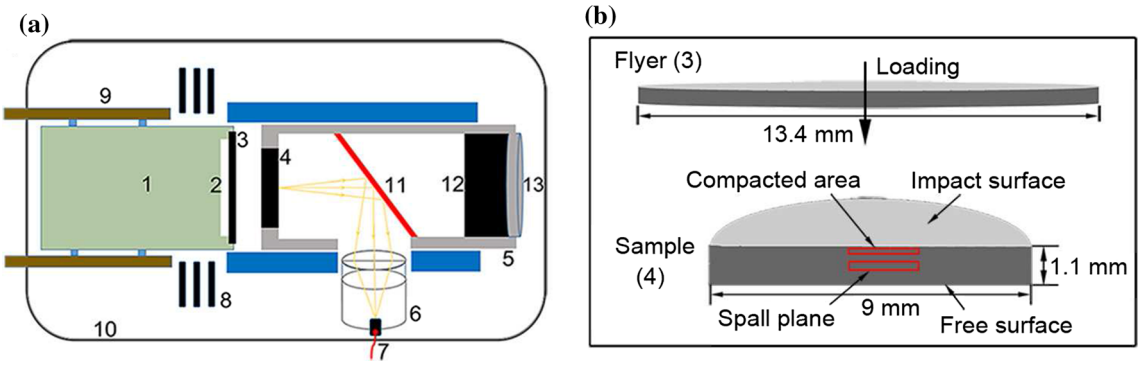

Figure 2 **a** Schematic setup of gas gun flyer plate impact experiments (not to scale). 1—polycarbonate sabot; 2—recess for release waves; 3—flyer plate; 4—sample; 5—recovery cylinder; 6—lens; 7—optical fiber connected to the photon Doppler velocimeter (PDV) probe; 8—optical fibers and detectors of the optical beam blocking system; 9—gun barrel; 10—vacuum chamber; 11—thin mirror; 12—soft recovery; 13—plug. **b** Dimensions of the flyer plate and sample. Impact surface, compacted region, spall region, and free surface are noted.

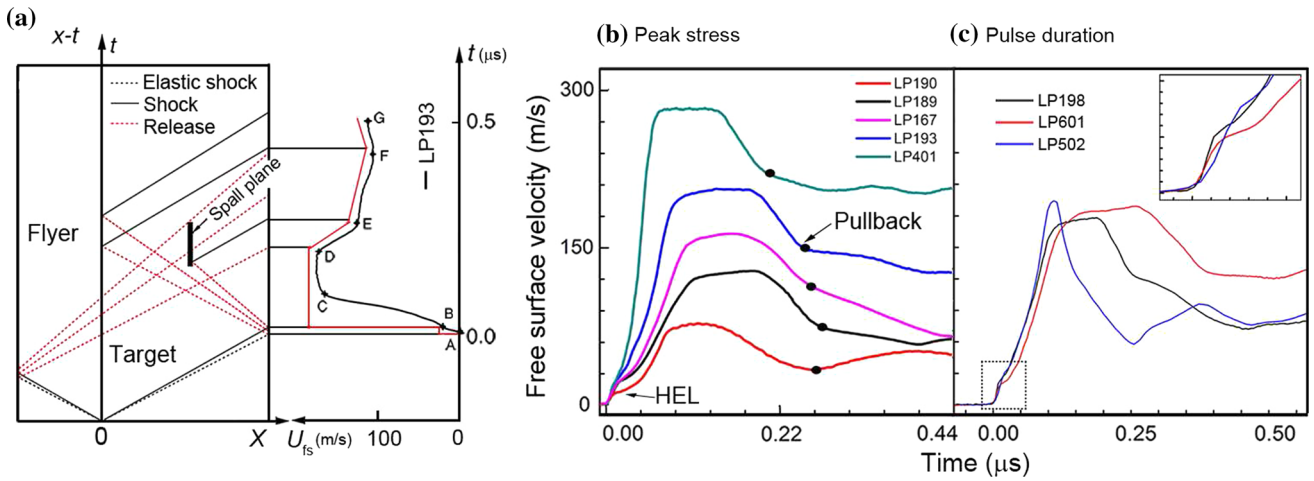

Figure 3 **a** Space–time or *x*–*t* diagram (left) and a corresponding free surface velocity history (right), illustrating wave propagation and interactions, showing shock, tension, spallation, and pullback. **b**, **c** Free surface velocity histories for the peak stress group and the pulse duration group, respectively.

A thin turning mirror (11) is used for relaying incoming and returning laser light, and minimizing the collateral damage for shock recovery. The shock-loaded target is "soft-recovered" for postmortem examinations (12). The flyer plate and sabot are blocked by the sample holder and separated from the sample after impact, in order to reduce collateral damage. The target then flies over a distance of ~ 30 cm into the soft matter and is protected from secondary impact. The recovered samples retain their original shape. The tilt of impact is 5 mrad as determined from multipoint PDV measurements, and the uncertainties in flyer plate and free surface velocity measurements are within 1%.

Disk-shaped flyer plates and targets are both made of the porous aluminum for symmetric impact to obtain the particle velocity conveniently. Two parallel surfaces of each flyer plate/target disk are polished to micron level or mirror finish. The diameters of the flyer plates and targets are 13.4 and 9 mm, respectively (Fig. 2b). Two groups of samples with different flyer plates and target thicknesses are prepared. For the peak stress group, the thicknesses are fixed and the impact or flyer plate velocity, u_f, is varied, while it is the opposite for the pulse duration group (Table 1).

All the samples are recovered from gas gun experiments and sectioned into two halves along the shock loading direction (Fig. 2b), ground and

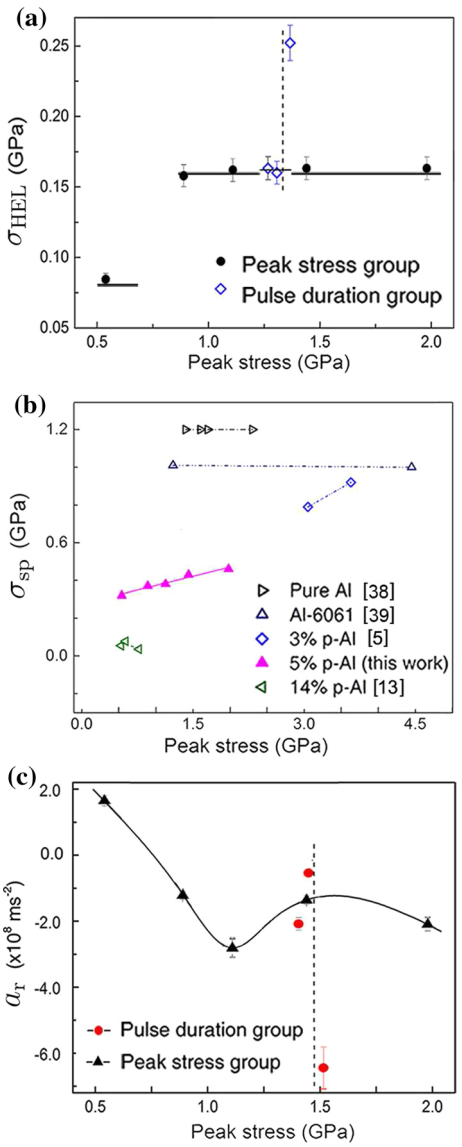

Figure 4 The Hugoniot elastic limit (**a**), spall strength (**b**), and re-acceleration due to pullback (**c**) as a function of peak stress. In **b**, literature results are included for comparison; p-Al refers to porous aluminum.

polished with 1- and 0.3-μm alumina particles, and then electro-polished in 10% perchloric acid and 90% alcohol at 28 V, with a Cu rod and the sample as electrodes. EBSD characterization is performed in a FEI Quanta 250 FEG-SEM equipped with Oxford EBSD detector and HKL channel 5 OIM software, with a 20 kV voltage, 15 mm working distance, and 70° tilt. Regions of interest for SEM and EBSD are in the central portion of the sample not affected by edge release.

Results and discussions

The flyer plate/target thickness ratios are approximately 1:2. Flyer plate velocity u_f ranges from 102 to 294 m s^{-1}, and peak stress (σ_H) varies from 0.54 to 1.98 GPa. The experimental parameters are summarized in Table 1. The space–time or x–t diagram is presented in Fig. 3a to illustrate wave propagation and interactions. Free surface velocity profiles, $u_{fs}(t)$, for the peak stress group and pulse duration group are shown in Fig. 3b, c, respectively.

Analysis of free surface velocity histories

We use the free surface velocity history labeled with A–G (shot LP193) in Fig. 3a, as well as the x–t diagram, to illustrate the HEL, dynamic compression, subsequent release, tension, and spallation. Segment AB indicates the elastic precursor, and B represents HEL. Plastic wave BC develops into a supported, stable shock, CD. The duration of the supported shock is defined as the loading pulse duration (τ). The arrival of the release fan (the red dashed line) from the back surface of the flyer plate leads to velocity drop (DE). The interaction of this release fan with that initiated from the target free surface gives rise to release and tension in the sample, and spallation is resulted when the tensile stress exceeds the tensile or spall strength (σ_{sp}) under a specific loading condition. The ensuing slope (EF) change in velocity is induced by the arrival of a compression wave originated from the spall plane within the sample. The re-acceleration beginning at E is a typical signature of spall, although the slope is still negative owing to the weak strength of spallation. EF is likely related to independent growth of isolated cracks or voids [12].

The velocity profiles, $u_{fs}(t)$, allow us to deduce such quantities as stress. For convenience, we use subscripts 0–2 to denote initial state, elastic precursor, and plastic shock, respectively. Following convention, we also use subscript H to denote a supported shock or Hugoniot state (state 2). U_s, u_p, and ρ denote shock wave velocity, shock-state particle velocity, and density, respectively. HEL stress [25] is given by:

$$\sigma_{HEL} = \rho_0 U_{s1} u_{p1} \approx \rho_0 C_1 u_{p1}. \quad (1)$$

The $U_s - u_p$ relation for the plastic shock wave is approximately described with that for a similar type of porous aluminum $U_s = C_0 + s u_p$, where $C_0 = 5.08$

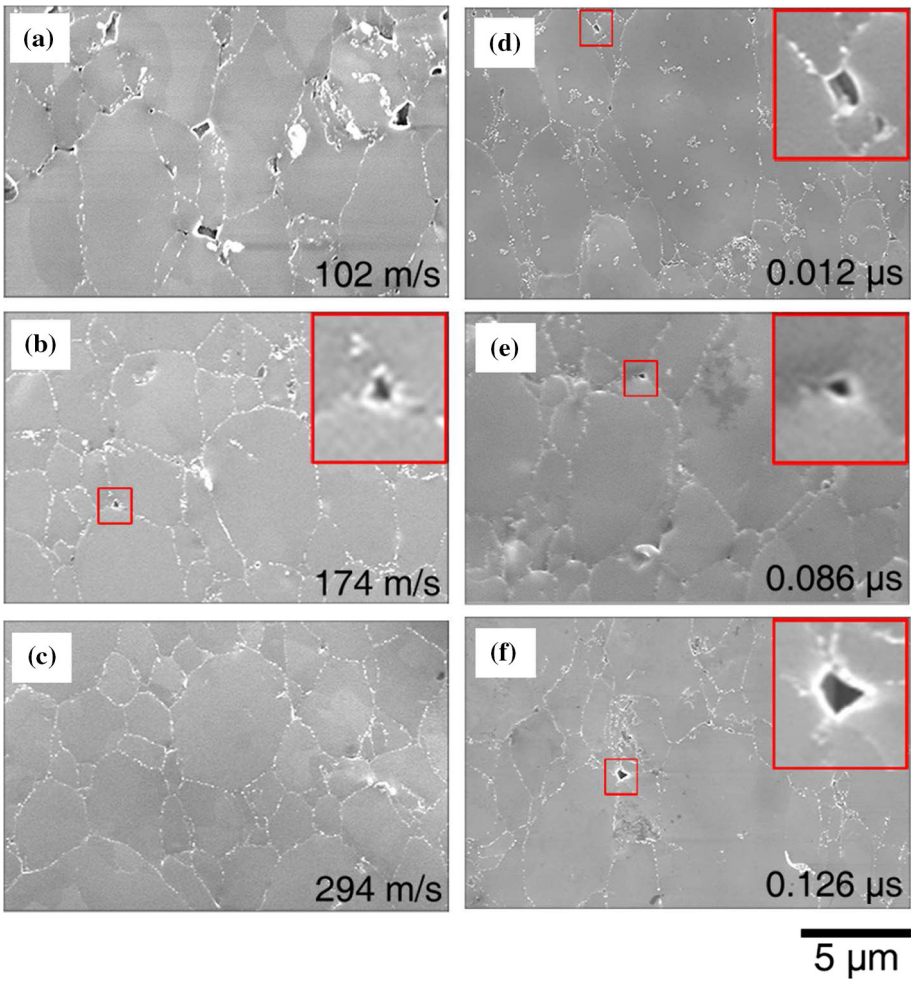

Figure 5 Shock compaction of preexisting voids: SEM micrographs of compacted areas for different impact velocities (**a**–**c**; peak stress group) and different flyer plate/target thicknesses (**d**–**f**; pulse duration group). The insets are magnified images corresponding to the regions indicated by smaller rectangles.

km s^{-1} and $s = 1.324$ [8]. For symmetric impact, u_p is half of the impact velocity. The peak shock stress is

$$\sigma_H = \sigma_{HEL} + \frac{\rho_0 U_{s1}}{U_{s1} - u_{p1}}[C_0 + s(u_{p2} - u_{p1})](u_{p2} - u_{p1})]. \quad (2)$$

Spall strength is calculated from the pullback velocity with the acoustic method [26, 27]

$$\sigma_{sp} \approx \rho_0 C_L \Delta u \frac{1}{1 + \frac{C_l}{C_b}}, \quad (3)$$

where the pullback velocity $\Delta u = u_{fs,D} - u_{fs,E}$.

On the basis of the geometric relationship indicated in Fig. 3a, the pullback in free surface velocity caused by the compression wave due to spallation occurs at $t_E = L_s/C_l$, where L_s is target thickness. These instants (E) are indicated by black dots in Fig. 3b for different impact velocities. The re-acceleration (EF) following the pullback, a_r, reflects the fracture rate [12, 28] and is quantified as

$$a_r = \frac{du_{fs}(t)}{dt}\Big|_{EF}. \quad (4)$$

The experimental parameters and results for two groups of experiments deduced from the free surface velocity measurements are collected in Table 1.

Effects of peak stress and pulse duration on HEL and spallation

Given preexisting micron- or submicron-sized voids, the apparent yield as indicated by HEL is a combined result of void collapse and crystal plasticity and therefore called pseudo-yield as well [18]. As shown in Fig. 3b, the elastic precursor steepens and HEL increases with increasing impact velocity for a given sample thickness (the peak stress group). This steepening is a manifestation of accelerated void collapse and material densification with increasing impact velocity and has been observed for a variety of porous/foam materials under shock loading

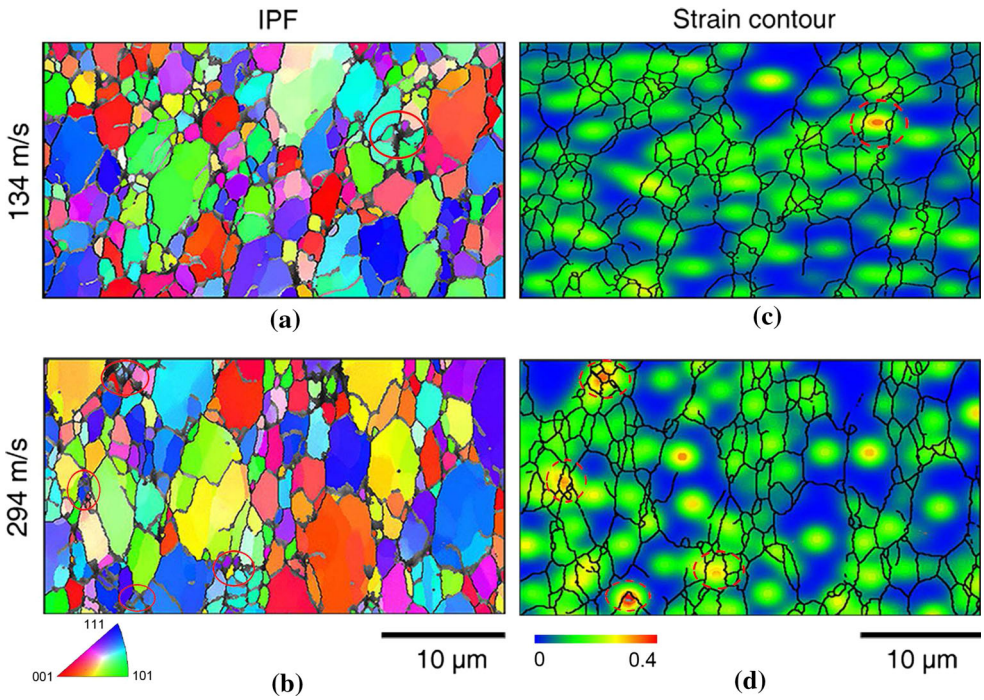

Figure 6 Shock compaction of preexisting voids: EBSD inverse pole figure maps overlaid with grain and particle boundaries in compacted areas (**a**, **b**), and corresponding strain contour maps (**c**, **d**).

[3, 13, 18]. The increase in HEL is characteristic of porous materials due to compaction-induced densification as well [13, 18], but it becomes saturated at an impact velocity of 134 m s^{-1} (Fig. 4a). On the other hand, increasing sample thickness leads to ramping elastic shock fronts and decreased HEL for similar impact velocities (the pulse duration group; Fig. 3c inset and Fig. 4a). This is similar to elastic precursor decay that has long been observed, e.g., for 1060 aluminum [29], steel [30], beryllium [31], and aluminum [32].

Therefore, the apparent yield point or HEL for porous aluminum depends initially on both sample thickness and impact velocity, but becomes saturated when their values become sufficiently large. Such a saturation represents a material property of aluminum, independent of sample dimension or impact strength. The maximum or stabilized HEL for this porous aluminum is $\sigma_{HEL} \approx 0.16$ GPa, consistent with a previous study on full-density aluminum (0.15 GPa) [33].

The spall strength of this low-porosity aluminum is plotted as a function of peak stress in Fig. 4b, together with literature results of pure aluminum [34], Al-6061 [35], 3% porous aluminum [3], and 14% porous aluminum [10] for comparison. Peak stress appears to have little influence on the spall strengths of full-density pure aluminum and Al-6061. However, spall strength of porous aluminum strongly depends on both peak stress and porosity. Spall strength decreases rapidly with increasing porosity at the same stress level, consistent with previous results [3, 10]. On the other hand, spall strength of porous aluminum increases linearly with peak stress, as a result of increasing compaction and thus decreasing porosity at higher peak stresses.

Figure 4c presents re-acceleration (a_r) [12, 28] as a function of peak stress. Contrary to full-density solids [12], a_r of porous materials can be negative, since spall strength is low and the compression wave initiated at spall plane is too weak to reverse the ongoing release of free surface velocity (Fig. 3a). In addition, this compression wave is attenuated by pores during propagation toward the free surface [3]. For the peak stress group, the re-acceleration exhibits two inflection points. The first inflection reflects a competition between compaction and tensile stress. The fracture rate decreases with increasing compaction, but increases with increasing tensile stress. The second decrease in a_r is attributed to a compaction-induced alteration of damage mechanisms (see Sect. 3.3.3). For the pulse duration group, a_r increases rapidly with increasing pulse duration, since longer pulse duration provides more time for damage nucleation and growth.

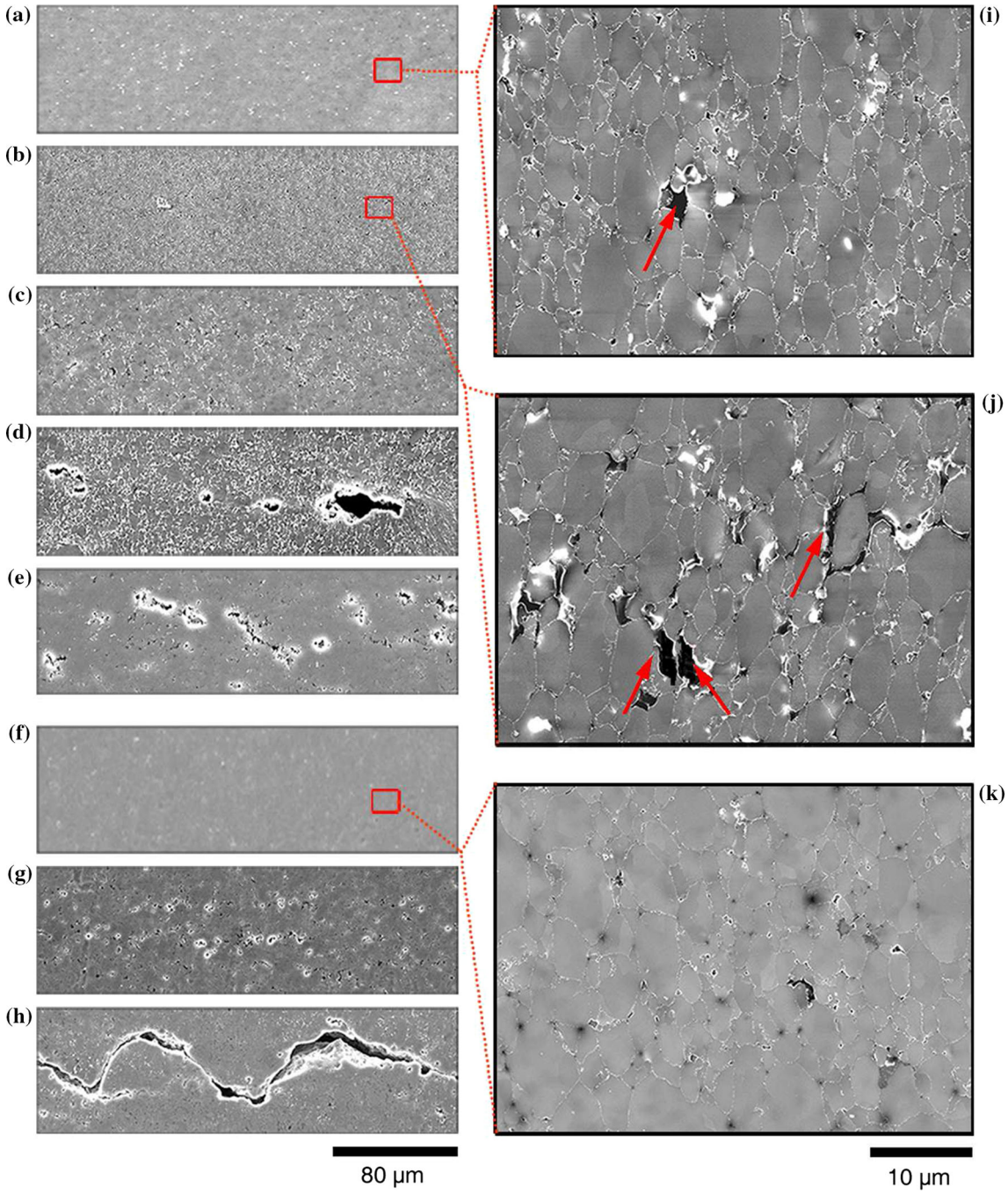

Figure 7 Spall damage: SEM micrographs for different impact velocities and pulse durations. **a**–**e** refer to the peak stress group and **f**–**h** the pulse duration group. **a**–**h** correspond to the shot numbers in Table 1 from top to bottom, i.e., LP190, LP189, LP167, LP193, and LP401, respectively. **h**–**k** are magnified areas noted with small rectangles. Impact direction: downward.

Microstructural analyses: deformation and fracture mechanisms

We perform SEM, EBSD, and XCT analyses of shock-recovered specimens to investigate impact-induced compaction, deformation, and spallation (Figs. 6, 7, 8, 9, 10, 11, 12). The region near the impact surface is examined as regards compaction of voids, while the spall region is analyzed primarily for spall damage, as indicated by the red rectangles in Fig. 2b.

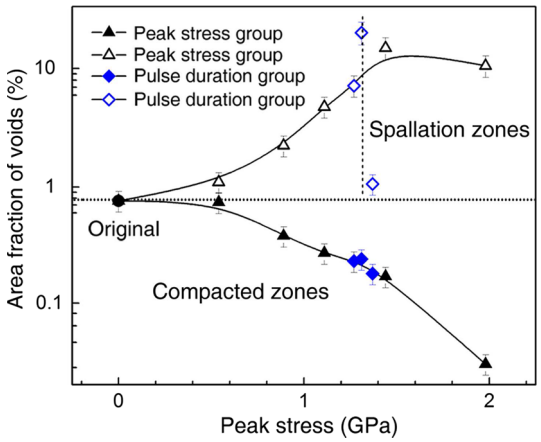

Figure 8 Area fractions of voids as a function of peak stresses obtained from SEM micrographs. Each data point is averaged from several measurements of different SEM graphs, and the error bars represent the standard deviations.

Dynamic compaction

SEM micrographs of the compacted regions of recovered samples under different impact velocities are shown in Fig. 5. For the peak stress group (Fig. 5a–c), the number and size of voids exhibit increasing reduction with the increase in impact velocity. The compacted area undergoes negligible modification for $u_f = 102$ m s^{-1} (Fig. 5a) compared to the as-received sample (Fig. 1a), while the voids almost disappear completely at 294 m s^{-1} (Fig. 6c). For the pulse duration group (Fig. 5d–f), the void morphology is similar at different pulse durations (as shown in the insets), indicating that pulse duration has insignificant effect on compaction compared to peak stress. The compacted voids are closed rather than healed and do not present a large resistance against subsequent tension, as manifested in Fig. 4 that the spall strength of porous Al is obviously lower than the fully dense Al.

Two representative inverse pole figures of the compacted regions are presented in Fig. 6a for $u_f =$ 102 m s^{-1} and in Fig. 6b for 294 m s^{-1} (the peak stress group). Little grain refinement is induced by shock compression. The strain contour maps corresponding to Fig. 6a, b are shown in Fig. 6c, d, respectively; these maps suggest that shock compression induces plastic strain localizations (indicated by dashed circles) around preexisting voids (solid circles). The number and amplitude of strain localizations increase with increasing impact velocity, consistent with shock-induced void collapse observed in Fig. 5, as well as steepening of elastic precursor in free surface velocity histories (Fig. 3). Shock-induced collapse of voids or pores can lead to temperature rise [36, 37], which increases with increasing shock pressure and porosity. In our experiments, the initial porosity is small (5%) and shock stress is low (below 2 GPa). So the temperature rise is mild according to molecular dynamics simulations on shock compaction of porous materials [37]. Overall, this low temperature rise is expected to have slight effect on microstructure at such short timescales.

Dynamic tensile fracture

The effects of peak stress and pulse duration on tensile damage and fracture are examined via 2D SEM and 3D XCT analyses (Figs. 7, 8, 9). The recovered specimens are sectioned into halves along the shock direction, and the cross-sections are analyzed with SEM. For XCT, rectangular parallelepiped samples are harvested from the spall region of the specimens, with a section area of 1.2 mm × 0.9 mm perpendicular to the spall plane and a height of 2 mm.

SEM micrographs in Fig. 7a–e refer to the peak stress group and those in Fig. 7f–h to the pulse duration group. Distributed voids and microcracks are observed in the spallation zone during dynamic tension, characteristic of ductile materials [22]. The magnified images (Fig. 7i, j) show clearly extended voids even under very low impact velocities (102 and 134 m s^{-1}). The damage extent increases with increasing impact velocity (Fig. 7c, d). However, the damage extent for $u_f = 294$ m s^{-1} (Fig. 7e) is lower than that for 213 m s^{-1} (Fig. 7d). For the pulse duration group, the number and size of voids in the spallation zones exhibit a significant increase with increasing pulse duration. Short pulse durations do not allow for the growth of initial and/or newly created voids so no obvious damage is observed across the sample (Fig. 7k), while longer pulse durations lead to bigger, isolated voids, or macroscopic cracks via growth and coalescence of isolated voids.

The area fraction of voids is obtained across the sample thickness from SEM micrographs (Figs. 5, 7) and shown as a function of peak stress in Fig. 8. At the compacted zone, the area fraction of voids is nearly identical to that of the as-received sample

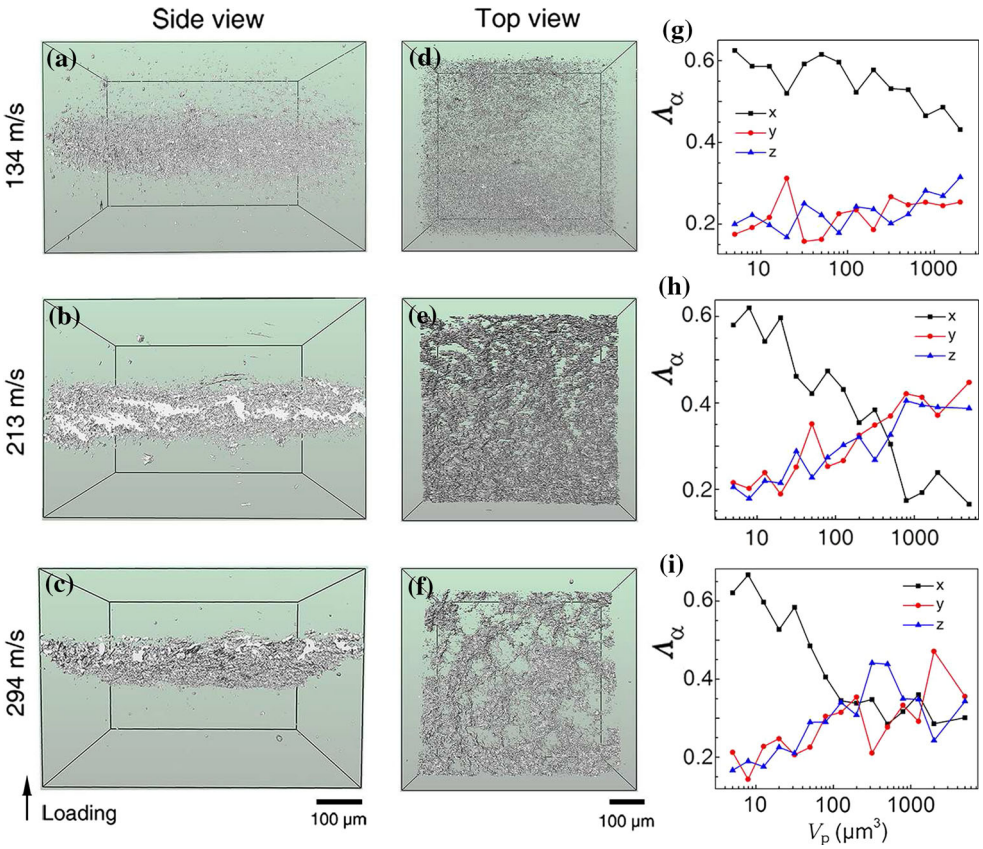

Figure 9 **a**–**f** X-ray tomography images of recovered samples at different impact velocities as labeled. **g**–**i** Orientation coefficient Λ_α of pores derived from **a**–**c**. The sampling volume is $500 \times 720 \times 700$ μm^3.

(negligible compaction) for a peak stress of 0.54 GPa (102 m s^{-1}). With increasing stress, this fraction decreases significantly due to compaction-induced void collapse to 0.03% at 1.98 GPa (essentially full density). In the spallation zone, the void fraction increases gradually with increasing stress up to 1.44 GPa, but exhibits slight decrease at higher stresses (see Sect. 3.3.3). Pulse duration has little influence on the void fraction in the compacted zone at similar peak stresses (blue solid diamonds, Fig. 8). However, the void fraction in the spallation zone increases significantly with increasing pulse duration. Longer pulse durations promote significantly damage nucleation and growth of porous aluminum, similar to the case of a mild steel [12].

3D microstructures of the recovered samples are also reconstructed with XCT. The void distributions are presented in Fig. 9a–f for three different impact velocities. Voids concentrate on the spall plane, where the amplitude and duration of tensile loading is the highest. The top-view images display a significant increase in voids growth and coalescence into microcracks at impact velocities above 213 m s^{-1}. However, the void/crack density at 294 m s^{-1} appears lower than that at 213 m s^{-1}, consistent with the SEM results (Fig. 8). This can be seen more clearly in accumulated volume distributions of voids across the sample (Fig. 10a). The void volume exhibits a quasi-Gaussian distribution and peaks around the spall plane [22, 38]. The peak void volume increases from 6.17×10^2 μm^3 at 134 m s^{-1} to 2.88×10^5 μm^3 at 213 m s^{-1}, but decreases to 1.08×10^5 μm^3 at 294 m s^{-1}. However, the width of void distributions decreases significantly with increasing impact velocities.

From 3D void configurations obtained with XCT, void or pore size distribution can be characterized in terms of $d_p(i)$, defined as [39]

$$d_p(i) = \frac{1}{10^i} \sum_{10^{i-1} \le V_p \le 10^i - 1} N_p(V_p), \tag{5}$$

where $N_p(V_p)$ is the number of pores with volume V_p located between 10^{i-1} μm^3 and 10^{i-1} μm^3. $d_p(i)$ obtained for different impact velocities is presented in Fig. 10b. The void size distributions after impact become much wider than that of the as-received sample, due to spall-induced void nucleation and

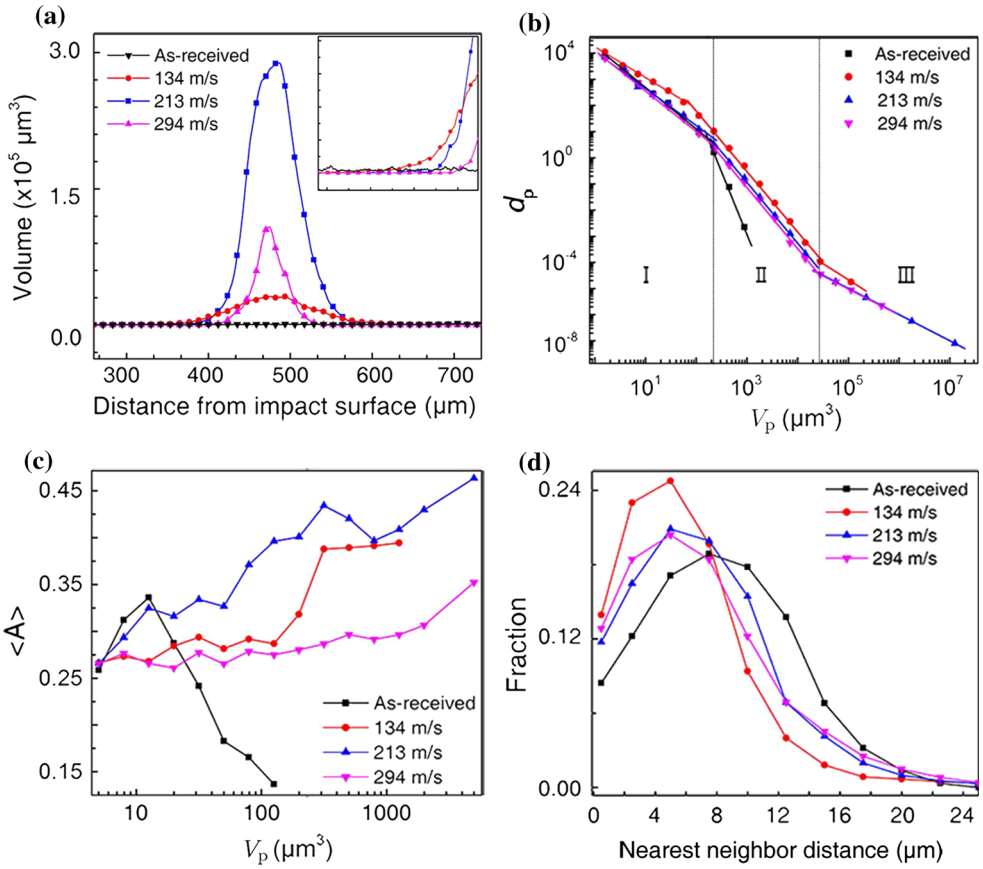

Figure 10 **a** Pore volume distribution as a function of distance away from the impact surface. **b** Number–size distribution of voids. **c** Average aspherical coefficient of pores. **d** Nearest-neighbor distance distributions. The estimated errors are ~ 1% for the volume calculations, ~ 4% for aspherical coefficients and ~ 1–2 μm for the nearest-neighbor distance.

growth. For shock-recovered samples, d_p can be described with three power laws (regimes I–III), i.e., $d_p \sim V_p^{-\tau}$, separated by two narrow transition zones centered at $V_p \approx 10^2$ and 10^4 μm^3.

For an impact velocity of 134 m s^{-1}, $\tau_I = 1.2$ in regime I, slightly lower than those for 213 m s^{-1} ($\tau_I = 1.5$) and 294 m s^{-1} ($\tau_I = 1.6$). However, τ is similar for different impact velocities in regime II ($\tau_{II} \approx 2.3$), but considerably higher than τ_I. τ_{III} (~ 1.0) is the lowest. These three regimes were also observed in spall damage of single-crystal tantalum via molecular dynamics simulations [40]. The differences in τ between different regimes are attributed to different void evolution modes during shock loading. Regime I represents nucleation and growth of voids, while regime II exhibits a faster decay (void number vs. volume), probably because of void coalescence which reduces void number but increases void size. Similarly, microcracking in regime III leads to a faster increase in pore volume than void number. Regime III for 134 m s^{-1} is narrow, and a possible reason is the premature termination of crack propagation as a result of low energy input. Early homogeneous void nucleation is not observed in the present study, probably owing to two reasons, preexisting voids (even after collapse) and the limited spatial resolution of XCT.

The topology of voids is also of interest and can be characterized with a gyration tensor G,

$$G_{\alpha\beta} = \frac{1}{V_p}\sum_{i=1}^{V_p}\left(r_{\alpha i}^{(p)} - r_{\alpha}^{(b)}\right)\left(r_{\beta i}^{(p)} - r_{\beta}^{(b)}\right), \quad (6)$$

where $r_{\alpha i}^{(p)}$ and $r_{\alpha}^{(b)}$ ($\alpha = x, y, z$) are coordinates of voxel i and of the barycentre (b) of pore p, respectively. V_p is the volume of pore p.

The eigenvalues R_i and associated eigenvectors $\varphi_{i,\alpha}$ of G are calculated for each pore. Then, we identify the largest R_i as R_{max}; the corresponding eigenvector φ_{max} is the orientation of R_{max}. We define $\Lambda_\alpha(V_p)$ as the probability that the maximum absolute value of the three components of φ_{max} is aligned with the α-axis. For instance, $\Lambda_x(V_p) > \Lambda_y(V_p)$ and $\Lambda_x(V_p) > \Lambda_z(V_p)$ mean that the pores with volume V_p are mainly oriented along the x-axis.

The orientation coefficients $\Lambda_\alpha(V_p)$ at different impact velocities are plotted in Fig. 9g–i. For small

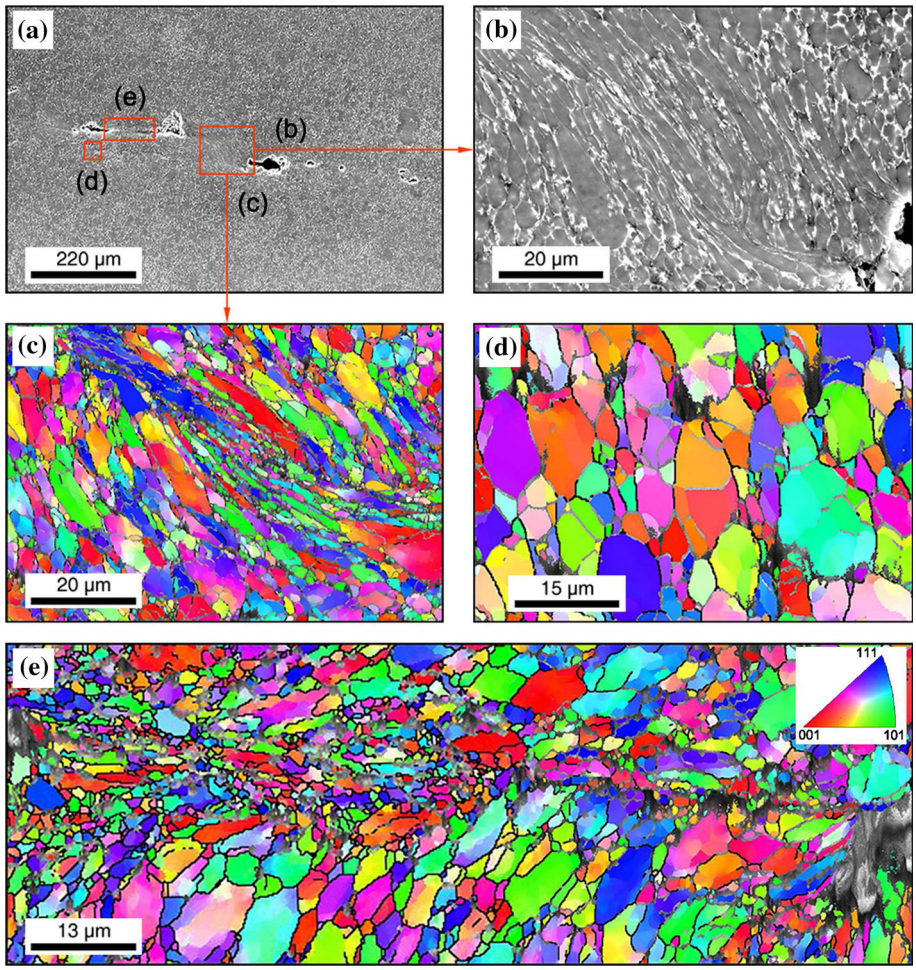

Figure 11 Cross-sectional SEM micrographs (**a**, **b**) and EBSD inverse pole figure maps (**c**–**e**), showing deformation modes in the spallation region for an impact velocity of 213 m s^{-1}. **b**, **c** refer to the same region. Impact direction: downward.

pores, Λ_x is much higher than Λ_y and Λ_z, indicating that small pores are mainly oriented along the x-axis, i.e., the shock direction or spall plane normal. With the increase in pore volume, Λ_x decreases while Λ_y and Λ_z increase (corresponding to regime II in Fig. 10b); the latter two curves for the transverse directions are similar despite different fluctuations. Thus, the probability is equal for small voids to grow and coalesce into big ones along the y- and z-axes, i.e., on the spall plane. Moreover, the decrease in Λ_x takes place earlier and appears to be more dramatic at high impact velocities than at 134 m s^{-1}. In the large pore range, Λ_x becomes even smaller than Λ_y and Λ_z for 213 m s^{-1}, while $\Lambda_x \approx \Lambda_y \approx \Lambda_z$ for 294 m s^{-1}. Therefore, void growth and coalescence develop preferentially along the y- and z-directions at 213 m s^{-1}, but simultaneously along x-, y-, and z-directions at 294 m s^{-1}. A possible reason is that trans-particle fracture occurs at 294 ms^{-1} and its propagation direction becomes unbiased, while only inter-particle fracture occurs at 213 m s^{-1} which mainly orients along lateral directions.

Damage evolution yields various pore shapes, which can be quantified with the aspherical coefficient defined as [40]

$$A = \frac{1}{2}\frac{\sum_{i>j}^{3}\left(R_i - R_j\right)^2}{\left(\sum_{i}^{3} R_i\right)^2}. \quad (7)$$

Here R_i (i = 1, 2, 3) are the eigenvalues of the gyration tensor defined in Eq. (6). For $R_1 \approx R_2 \approx R_3$, $A \approx 0$, corresponding to a quasi-spherical pore. An increase in A indicates an increasing inequality among the three eigenvalues, i.e., the three axes of an ellipsoidal pore.

The average aspherical coefficient distributions of voids for the as-received and shock-recovered samples are presented in Fig. 10c. For the as-received sample, small pores are mainly oblate ellipsoids, while large pores are increasingly closer to spheres

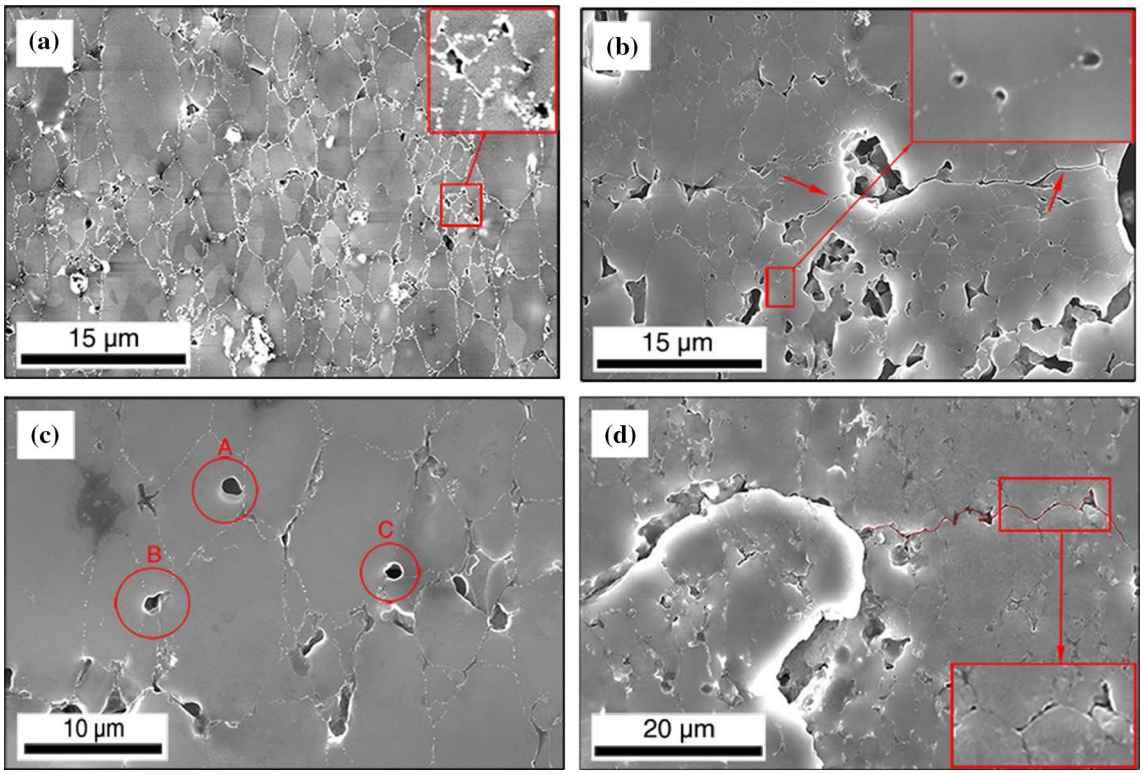

Figure 12 SEM micrographs showing damage modes at different impact velocities and durations. **a** 102 m s^{-1}, **b** 213 m s^{-1}, and **c** 294 m s^{-1} in the peak stress group. **d** 194 m s^{-1} in the pulse duration group ($\tau = 126$ ns).

with increasing size. The aspherical coefficients of pores after impact increase with increasing pore size, in contrast to the trend for the as-received material. Thus, pores are generally more ellipsoidal at larger sizes, due to transverse growth and coalescence of small voids along the *y*- and *z*-directions (Fig. 9), consistent with regime II (Fig. 10b). However, at the same pore size, the aspherical coefficient firstly increases with the impact velocity but then decreases significantly at 294 m s^{-1}. The pores are the most ellipsoidal at 213 m s^{-1}, but becomes more spherical at 294 m s^{-1}, consistent with the SEM micrographs in Fig. 7.

We also calculate the nearest-neighbor distance distributions of voids for the as-received and shock-recovered samples. The initial pore distance is mainly around 8 μm comparable to the average particle size, since pores form at the particle junctions. At 134 m s^{-1}, the distribution curve shifts leftward, indicating a decrease in the average distance between neighboring pores, because original voids grow bigger and new voids are also nucleated. For higher impact velocities, the fraction of pores at small nearest-neighbor distances decreases due to compaction, while the fraction of pores at larger distances increases due to void coalescence. Compared to the as-received material, the average neighbor distance of voids decreases after shock loading, indicating increasing interactions between them.

Microscopic deformation and fracture modes

Deformation modes of this sintered aluminum during shock loading are discussed with SEM and EBSD micrographs of shock-recovered samples (Fig. 11), using the case of 213 m s^{-1} as an example. Figure 11b, c shows significant shear deformation and grain refinement between two staggered microcracks. Particles and grains are markedly elongated along a direction $\sim 40°$ from the impact direction, similar to shear bands observed in steel [41] and Ti–6Al–4V alloy [42]. However, the area between two cracks aligned horizontally exhibits considerable grain refinement only, with little shear deformation (Fig. 11e). Little grain refinement and plastic deformation are observed in the area away from the void pairs (Fig. 11d). Therefore, shear strain localization is attributed to tension-induced shear stress

concentration at crack tips which alters the local stress state between them [43], i.e., void/crack interactions. Voids and cracks tend to grow and propagate along such localized plastic zones [44]. That explains why the spall plane (Fig. 7h) appears to be wavy at ~ 100 μm scale and the cracking inclined angle is similar to the shear deformation angle here, i.e., ~ 40°.

The characteristic damage/fracture modes of sintered aluminum are presented in Fig. 12. At 102 m s^{-1}, voids or microcracks are found mostly around the junctions of multiple (≥ 3) particles (Fig. 12a inset) where voids tend to form even during sintering (Fig. 1a) and thus serve as nucleation sites of damage. Extended cracks is not observed since the peak stress is low.

At 213 m s^{-1}, some of the original voids collapse (Fig. 8b), and the survived ones grow into microcracks propagating preferentially along particle boundaries (marked by arrows), which are inherently weaker than the particle matrix. Coalesced cracks along particle boundaries are shown more clearly in Fig. 12d, for a slightly lower impact velocity (194 m s^{-1}) but much longer pulse durations (126 ns). This inter-particle fracture is common in sintered metal composites and ceramics [45, 46]. Apart from growth of the original voids, tiny voids (1–2 μm) nucleate at triple particle junctions (Fig. 12b inset), since the bond strength of triple particle junctions is generally weaker than double-particle boundaries and particle matrix [45], even after original voids are compacted at such junctions.

At the highest impact velocity (294 m s^{-1}), full density is essentially achieved during shock compression (Fig. 5e). Upon subsequent dynamic tension, growth of initial voids becomes negligible, while random nucleation of new voids at particle boundaries, and even within particle interiors, prevails. Few extended cracks are observed across the sample due to strengthening via compaction, consistent with considerable reduction in re-acceleration a_r and damage extent (Figs. 4c, 7e). At low peak stresses, damage only occurs in weak zones (Fig. 12a), but both weak and strong zones are damaged at sufficiently high peak stresses, to accommodate the strain imposed by high loading rates (Fig. 12c). This is also responsible for the increase in spall strength with increasing peak stress (Fig. 4b).

Summary

We conduct plate impact experiments to investigate deformation and spall damage of low-porosity aluminum. Free surface velocity histories are measured, and the Hugoniot elastic limit and spall strengths are derived. SEM, EBSD, and XCT are used to characterize 2D and 3D microstructures.

3D void topology analyses yield rich information on size distribution, shape, orientation, and connectivity of voids. The void size distributions exhibit three regimes, all of which can be described with power laws; the powers in different regimes reflect a transition of void evolution modes during shock loading, from void nucleation/growth to coalescence and propagation in sequence. Small voids are mainly oriented along the shock direction, but subsequent growth and coalescence allow them to develop transversely with increasing impact velocity.

HEL decreases/increases with sample thickness/impact velocity and approaches saturation, while tensile strength increases with increasing peak stress and shock-induced densification. With increasing compaction under increasing impact velocities, spall damage modes change from growth of original voids to inter-particle crack propagation and to "random" nucleation of voids. Such a change in damage mechanism also gives rise to a distinct decrease in damage extent at high impact velocities. Compaction induces strain localizations around the original voids, while subsequent tension results in grain refinement, and shear deformation zones between staggered cracks.

Acknowledgements

We are grateful for the support by the National Key R&D Program of China (2017YFB0702002), NSAF (U1330111), NSFC (11627901), and the Scientific Challenges Project of China. Use of the Advanced Photon Source, an Office of Science User Facility operated for the US Department of Energy (DOE) Office of Science by Argonne National Laboratory, was supported by the US DOE under Contract no. DE-AC02-06CH11357.

References

[1] Liu YB, Lim SC, Lu L, Lai MO (1994) Recent development in the fabrication of metal matrix-particulate composites using powder metallurgy techniques. J Mater Sci 29(8):1999–2007. https://doi.org/10.1007/BF01154673

[2] Cavaliere P, Sadeghi B, Shabani A (2017) Carbon nanotube reinforced aluminum matrix composites produced by spark plasma sintering. J Mater Sci 52(14):8618–8629. https://doi.org/10.1007/s10853-017-1086-6

[3] Wang YG, He HL, Qi ML, Shen L, Bai B (2007) Time-resolved dynamic compaction and tensile fracture of low-porosity aluminum under impact loading. J Appl Phys 102(7): 073518

[4] Victoria M, Baluc N, Bailat C, Dai Y, Luppo MI, Schaublin R, Singh BN (2000) The microstructure and associated tensile properties of irradiated fcc and bcc metals. J Nucl Mater 276(1):114–122

[5] San Marchi C, Mortensen A (2001) Deformation of open-cell aluminum foam. Acta Mater 49(19):3959–3969

[6] Mao XH (2013) Dynamic response of the compound structure of foam aluminum core composite sandwich material to the shock wave of gas explosion. Adv Mater Res 690: 1149–1157

[7] Farrell K (1981) Microstructure and tensile properties of heavily irradiated 5052–0 aluminum alloy. J Nucl Mater 97(1–2):33–43

[8] Song P, Cai LC, Wang QS, Zhou XM, Li XZ, Zhang Y, Yuan S, Weng JD, Li JB (2011) Sound velocity, temperature, melting along the Hugoniot and equation of state for two porosity aluminums. J Appl Phys 110(10):103522

[9] Wang Y, Qi M, He H, Wang L (2014) Spall failure of aluminum materials with different microstructures. Mech Mater 69(1):270–279

[10] Kraus RG, Chapman DJ, Proud WG, Swift DC (2009) Hugoniot and spall strength measurements of porous aluminum. J Appl Phys 105(11):114914

[11] Xiao Y, Liu H, Chen Q, Long L, Xiang J (2017) Evolution of particle breakage and volumetric deformation of binary granular soils under impact load. Granul Matter 19(4):71–81

[12] Li C, Li B, Huang JY, Ma HH, Zhu MH, Zhu J, Luo SN (2016) Spall damage of a mild carbon steel: effects of peak stress, strain rate and pulse duration. Mater Sci Eng A 660:139–147

[13] Bonnan S, Hereil PL, Collombet F (1998) Experimental characterization of quasi static and shock wave behavior of porous aluminum. J Appl Phys 83(11):5741–5749

[14] Ifergane S, Barkay Z, Beeri O, Eliaz N (2010) Study of fracture evolution in copper sheets by in situ tensile test and EBSD analysis. J Mater Sci 45(23):6345–6352. https://doi.org/10.1007/s10853-010-4596-z

[15] Lu L, Huang JW, Fan D, Bie BX, Sun T, Fezzaa K, Gong XL, Luo SN (2016) Anisotropic deformation of extruded magnesium alloy AZ31 under uniaxial compression: a study with simultaneous in situ synchrotron X-ray imaging and diffraction. Acta Mater 120:86–94

[16] Patterson BM, Henderson K, Smith Z (2013) Measure of morphological and performance properties in polymeric silicone foams by X-ray tomography. J Mater Sci 48(5):1986–1996. https://doi.org/10.1007/s10853-012-6965-2

[17] Tran H, Doumalin P, Delisee C, Dupre J, Malvestio J, Germaneau A (2013) 3D mechanical analysis of low-density wood-based fiberboards by X-ray microcomputed tomography and digital volume correlation. J Mater Sci 48(8):3198–3212. https://doi.org/10.1007/s10853-012-7100-0

[18] Li T, Fan D, Lu L, Huang JY, E JC, Zhao F, Qi ML, Sun T, Fezzaa K, Xiao XH, Zhou XM, Suo T, Chen W, Li YL, Zhu MH, Luo SN (2015) Dynamic fracture of C/SiC composites under high strain-rate loading: microstructures and mechanisms. Carbon 91:468–478

[19] Escobedo JP, Brown EN, Trujillo CP, Cerreta EK, Gray GT III (2013) The effect of shock-wave profile on dynamic brittle failure. J Appl Phys 113(10):103506

[20] Xiao Y, Stuedlein A, Chen Q, Liu H, Liu P (2017) Stress-strain-strength response and ductility of gravels improved by polyurethane foam adhesive. J Geotech Geoenviron Eng 10. https://doi.org/10.1061/(ASCE)GT.1943-5606.0001812

[21] Yang Z, Maurey A, Kang J, Wilkinson DS (2016) 2D and 3D characterization of pore defects in die cast AM60. Mater Charact 114:254–262

[22] Qi ML, Yao Y, Bie BX, Ran XX, Ye W, Fan D, Li P (2015) Nucleation and growth of damage in polycrystalline aluminum under dynamic tensile loading. AIP Adv 5(3):037116

[23] Huang JY, Li Y, Liu QC, Zhou XM, Liu LW, Liu CL, Zhu MH, Luo SN (2015) Origin of compression-induced failure in brittle solids under shock loading. Phys Rev B 92(14):144101

[24] Strand OT, Goosman D, Martinez C, Whitworth T, Kuhlow W (2006) Compact system for high-speed velocimetry using heterodyne techniques. Rev Sci Instrum 77(8):083108

[25] Arman B, Luo SN, Germann T, Cagin T (2010) Dynamic response of $Cu_{46}Zr_{54}$ metallic glass to high-strain-rate shock loading: plasticity, spall, and atomic-level structures. Phys Rev B 81(14):144201

[26] Antoun T, Curran DR, Razorenov SV, Seaman L, Kanel GI, Utkin AV (2003) Spall fracture. Springer, New York

[27] Luo SN, An Q, Germann TC, Han LB (2009) Shock-induced spall in solid and liquid Cu at extreme strain rates. J Appl Phys 106(1):013502

[28] Kanel GI, Razorenov SV, Bogatch A, Utkin AV, Grady DE (1997) Simulation of spall fracture of aluminum and magnesium over a wide range of load duration and temperature. Int J Impact Eng 20(6):467–478

[29] Arvidsson TE, Gupta YM, Duvall GE (1975) Precursor decay in 1060 aluminum. J Appl Phys 46(10):4474–4478

[30] Wang YG, He HL, Wang LL (2010) Experimental investigation of precursor decay in shock compressed mild steel by the VISAR interferometry technique. Strain 46(3):298–301

[31] Adams CD, Anderson WW, Blumenthal WR, Gray GT III (2014) Elastic precursor decay in S-200F beryllium. In: Journal of physics: conference series, vol 500, p 112001

[32] Whitley VH, McGrane SD, Eakins DE, Bolme CA, Moore DS, Bingert JF (2011) The elastic-plastic response of aluminum films to ultrafast laser-generated shocks. J Appl Phys 109(1):013505

[33] Huang H, Asay JR (2005) Compressive strength measurements in aluminum for shock compression over the stress range of 4–22 GPa. J Appl Phys 98(3):033524

[34] Qi ML, He HL, Yan SL (2007) Measurement and analysis of spall characteristics of high-pure aluminium at one-dimensional strain loading. Chin Phys Lett 24(8):2338–2340

[35] Stevens AL, Tuler FR (1972) Effect of shock precompression on the dynamic fracture strength of 1020 steel and 6061 T6 aluminum. J Appl Phys 42(13):5665–5670

[36] Zhao FP, Li B, Jian WR, Wang L, Luo SN (2015) Shock-induced melting of honeycomb-shaped Cu nanofoams: effects of porosity. J Appl Phys 118(3):035904

[37] Jian WR, Li B, Wang L, Yao XH, Luo SN (2015) Shock response of open-cell nanoporous Cu foams: effects of porosity and specific surface area. J Appl Phys 118(16): 165902

[38] Brown AD, Pham Q, Peralta P, Luo SN, Patterson BM, Byler D, Koskelo A, Xiao X (2015) Correlations between spall damage mode preference and microstructure in shocked polycrystalline copper: a 3-D X-ray tomography study. J Dyn Behav Mater 1(4):388–396

[39] Bontaz-Carion J, Pellegrini Y-P (2006) X-ray microtomography analysis of dynamic damage in tantalum. Adv Eng Mater 8(6):480–486

[40] Soulard L, Bontaz-Carion J, Cuq-Lelandais JP (2012) Experimental and numerical study of the tantalum single crystal spallation. Eur Phys J B 85(10):1–15

[41] Hartley K, Duffy J, Hawley R (1987) Measurement of the temperature profile during shear band formation in steels deforming at high strain rates. J Mech Phys Solids 35(3):283–301

[42] Xue Q, Meyers MA, Nesterenko VF (2002) Self-organization of shear bands in titanium and Ti–6Al–4V alloy. Acta Mater 50(3):575–596

[43] Packard C, Schuh C (2007) Initiation of shear bands near a stress concentration in metallic glass. Acta Mater 55(16):5348–5358

[44] Traiviratana S, Bringa EM, Benson DJ, Meyers MA (2008) Void growth in metals: atomistic calculations. Acta Mater 56(15):3874–3886

[45] Kim D-K, Lee S, Noh J-W (1998) Dynamic and quasi-static torsional behavior of tungsten heavy alloy specimens fabricated through sintering, heat-treatment, swaging and aging. Mater Sci Eng A 247(1):285–294

[46] Kovalčíková A, Dusza J, Šajgalík P (2009) Thermal shock resistance and fracture toughness of liquid-phase-sintered SiC-based ceramics. J Eur Cerm Soc 29(11):2387–2394